



# Image-based computational assessment of vascular wall mechanics and hemodynamics in pulmonary arterial hypertension patients



Byron A. Zambrano<sup>a</sup>, Nathan A. McLean<sup>a</sup>, Xiaodan Zhao<sup>b</sup>, Ju-Le Tan<sup>b</sup>, Liang Zhong<sup>b,c</sup>, C. Alberto Figueroa<sup>d</sup>, Lik Chuan Lee<sup>a</sup>, Seungik Baek<sup>a,\*</sup>

<sup>a</sup> Department of Mechanical Engineering, Michigan State University, 2555 Engineering Building, East Lansing, MI 48824, USA

<sup>b</sup> National Heart Center, 5 Hospital Dr, Singapore 169609, Singapore

<sup>c</sup> Duke-NUS Medical School, 8 College Road, Singapore 169857, Singapore

<sup>d</sup> Departments of Biomedical Engineering and Surgery, University of Michigan, 2800 Plymouth Road, NCRC B20-211W, Ann Arbor, MI 48105, USA

## ARTICLE INFO

### Article history:

Accepted 17 December 2017

### Keywords:

Hemodynamics  
Fluid-structure interaction  
Pulmonary arterial hypertension  
Finite element modeling

## ABSTRACT

Pulmonary arterial hypertension (PAH) is a disease characterized by an elevated pulmonary arterial (PA) pressure. While several computational hemodynamic models of the pulmonary vasculature have been developed to understand PAH, they are lacking in some aspects, such as the vessel wall deformation and its lack of calibration against measurements in humans. Here, we describe a computational modeling framework that addresses these limitations. Specifically, computational models describing the coupling of hemodynamics and vessel wall mechanics in the pulmonary vasculature of a PAH patient and a normal subject were developed. Model parameters, consisting of linearized stiffness  $E$  of the large vessels and Windkessel parameters for each outflow branch, were calibrated against *in vivo* measurements of pressure, flow and vessel wall deformation obtained, respectively, from right-heart catheterization, phase-contrast and cine magnetic resonance images. Calibrated stiffness  $E$  of the proximal PA was 2.0 and 0.5 MPa for the PAH and normal models, respectively. Calibrated total compliance  $C_T$  and resistance  $R_T$  of the distal vessels were, respectively, 0.32 ml/mmHg and 11.3 mmHg\*min/l for the PAH model, and 2.93 ml/mmHg and 2.6 mmHg\*min/l for the normal model. These results were consistent with previous findings that the pulmonary vasculature is stiffer with more constricted distal vessels in PAH patients. Individual effects on PA pressure due to remodeling of the distal and proximal compartments of the pulmonary vasculature were also investigated in a sensitivity analysis. The analysis suggests that the remodeling of distal vasculature contributes more to the increase in PA pressure than the remodeling of proximal vasculature.

© 2017 Elsevier Ltd. All rights reserved.

## 1. Introduction

Clinically, pulmonary arterial hypertension (PAH) is defined by an elevated mean pulmonary arterial pressure (mPAP) that is greater than 25 mmHg with left atrial pressure or in the presence of a pulmonary capillary wedge pressure less than 15 mmHg (McLaughlin et al., 2009). Among the numerous pathological features accompanying the increase in mPAP in PAH patients include the proliferation and migration of vascular smooth muscle cells, thickening of intima and media, development of plexiform lesions in small to medium size pulmonary arteries, and stiffening of large

pulmonary vessels (Shimoda and Laurie, 2013; Sutendra and Michelakis, 2013).

Although several animal models such as chronic hypoxia or monocrotaline rat models have been used to understand the pathogenesis of PAH, there are currently no animal models that can completely replicate human PAH (Shimoda and Laurie, 2013; Stenmark et al., 2009). This issue is exacerbated by the fact that vascular tissue samples from PAH patients are scarce, whereas studies using these samples have mostly been confined to small-scale biochemical and histological measurements (Tuder et al., 2007) that provide only limited insights on the organ-level alterations of vessel wall mechanics and hemodynamics in this disease. Furthermore, regional changes in vessel wall mechanics and hemodynamics are obscured in global measurements of pressure waveforms from right heart catheterization (RHC), the current gold standard for diagnosing PAH. This disconnect in data acquired

\* Corresponding author at: Department of Mechanical Engineering, Michigan State University, 2555 Engineering Building, East Lansing, MI 48824, USA.  
E-mail address: [sbaek@egr.msu.edu](mailto:sbaek@egr.msu.edu) (S. Baek).

across different scales may be addressed by developing physics-based computational models that are calibrated against experimental and/or clinical measurements.

Computational models of PAH hemodynamics have received considerably less attention than their systemic vasculature counterparts (Kheyfets et al., 2015; Su et al., 2013, 2012; Tang et al., 2012). These models, albeit useful in gaining insights on the different biomechanical aspects of PAH, present either of the following limitations: (1) a rigid wall modeling assumption (a critically important limitation considering that tissue stiffness is a key parameter of the problem) in patient-specific anatomical models (Kheyfets et al., 2015; Tang et al., 2012), (2) fluid-structure interaction formulations performed on highly idealized geometries (Su et al., 2013, 2012). Furthermore, to the best of our knowledge, no contribution has thus far been made to simultaneously calibrate 3D models of PAH against measurements of blood flow and vessel wall mechanics (Hunter et al., 2006; Kheyfets et al., 2013).

In this work, we present a computational model of pulmonary vasculature hemodynamics that seeks to overcome the aforementioned limitations. This model not only accounts for the fluid-structure interactions between blood flow and vessel wall in patient-specific anatomical models, but more importantly, is calibrated against patient-specific data of vessel wall deformation and hemodynamics. This approach enables the incorporation of large vessels stiffness, as well as the compliance and resistance of the distal vessels in a patient-specific manner. We present results derived from a PAH patient and a normal subject. The calibrated models were then used to isolate and quantify the contribution of mechanical changes in the distal (small vessels) and proximal (large vessels) compartments to the increase in mPAH found in PAH patients. The approach described here lays the foundation for subsequent development of patient-specific computational hemodynamics models of PAH.

## 2. Methods

### 2.1. PAH subject data

Cine and phase-contrast (PC) magnetic resonance (MR) images were acquired (using a 3-Tesla Philips scanner with ECG gating) from a 44-year-old PAH male subject. Main pulmonary artery (MPA) blood velocities and volumetric flow were computed from the PC-MR images using Q-Flow software (Philips Medical Systems). Right-heart catheterization was performed within 1 week of the imaging examination to measure pressure waveforms in the MPA. On the other hand, cine MR images of a 65-year old volunteer with no known cardiovascular disease (from a separate dataset) was also used here to develop computational hemodynamics model of a normal pulmonary vasculature. All data were acquired at the National Heart Center of Singapore, and both subjects gave written informed consent.

### 2.2. Estimation of pressure and flow in the normal subject MPA

Phase-contrast and RHC data were not available for the 65 years old normal subject. To address this issue, pressure and volumetric flow waveforms acquired in a previous study on healthy subjects (Lankhaar et al., 2006) were used here as surrogate data for the normal subject of this study. We note here that the normal subject was well within the  $54 \pm 16$  years old age-range of the subjects found in that study. The surrogate volumetric flow waveform was scaled so that the total outflow volume per cycle was equal to the subject-specific right ventricular stroke volume measured from the cine MR images.

### 2.3. Pressure-displacement relationship in the MPA

Pressure-displacement relationship of the MPA was established from the cine MR images and the pressure waveform in both subjects. Specifically, cross-sectional area of the proximal MPA ( $A_{MPA}$ ) was measured over time and its equivalent diameter was calculated as  $D_{MPA}(t) = \sqrt{\frac{4}{\pi}A_{MPA}(t)}$ . We note here that the equivalent diameter is a commonly used metric in clinical practice in most cardiovascular diseases (Bellinazzi et al., 2015; Gharahi et al., 2015; Jakrapanichakul and Chirakarnjanakorn et al., 2011). Using end-diastolic (ED) diameter  $D_{MPA}(t_{ED})$  as a reference, time-resolved MPA radial displacement was estimated as  $\Delta D_{MPA}(t) = D_{MPA}(t) - D_{MPA}(t_{ED})$ . The radial displacement waveform  $\Delta D_{MPA}(t)$  was synchronized with the pressure waveform  $P(t)$  to derive the pressure-displacement relationship  $P(\Delta D_{MPA})$ .

### 2.4. Finite element model of the pulmonary vasculature

Geometry consisting of up to the first 4 generations of branches in the pulmonary vasculature was reconstructed from cine MR images acquired at ED in the PAH patient and normal subject. The geometry includes the MPA, left pulmonary artery (LPA) and right pulmonary artery (RPA). Reconstruction of the PA geometries was performed using MeVisLab ([www.mevislab.de](http://www.mevislab.de)). These geometries were subsequently refined and meshed using CRIMSON (Cardiovascular Integrated Modelling and Simulation; [www.crimson.software](http://www.crimson.software); Khlebnikov and Figueroa, 2015). An anisotropic mesh with characteristic element sizes varying from 0.7 mm in the center of the lumen to 0.3 mm at the first five boundary layers adjacent to the lumen surface of each vessel was generated in both geometries. This choice, which gives a good balance between accuracy and computational speed, was based on a mesh convergence study that is similar to Kheyfets et al. (2015). Details of this analysis is given in Appendix A. The resultant meshes for the PAH and normal models contain approximately 2.8 and 2 million elements, respectively. A summary of data used in calibration and construction of the two models is given in Table 1.

### 2.5. Simulation of hemodynamics and wall deformation in the pulmonary arteries

Hemodynamic simulations based on a coupled momentum formulation (Figueroa et al., 2006) that accounts for the fluid-structure interaction between blood flow and the arterial wall deformation (Xiao et al., 2013) were performed on the PAH and normal models. This formulation, which was implemented in CRIMSON's stabilized finite element solver, has been validated against experimental/clinical measurements (Cuomo et al., 2017, 2015) and deformable phantoms of the aorta (Kung et al., 2011). In the coupled momentum formulation, blood was assumed to behave as a Newtonian fluid with a prescribed viscosity  $\eta$ , whereas the arterial wall was assumed to behave as a linear isotropic elastic membrane with prescribed linearized stiffness  $E$ , Poisson ratio  $\nu$  and wall thickness  $h$ . Local values of wall thickness were estimated using a diameter-thickness ratio (1:0.019) found in morphometric studies on large pulmonary arteries of rats (Hislop and Reid, 1978) that was adjusted accordingly to the diameter and thickness measured in humans (Trip et al., 2015). Poisson ratio  $\nu = 0.5$  was prescribed in both models. The inlet and outlets rings of all vessels in the models were kept fixed in the simulations.

Measured and surrogated volumetric flow waveforms were mapped to a blunt and parabolic velocity profile that was imposed as boundary condition at the MPA inlet in the PAH and normal models, respectively. Each outlet was coupled to a three-element Windkessel model parameterized by  $R_1$ ,  $R_2$  and  $C$ , representing

**Table 1**  
Summary of data and information used for calibrating the normal and PAH model.

	Age (years)	Cardiac index (L/min/m <sup>2</sup> )	Volumetric flow waveform	Pressure waveform	3D computational model	Diameter changes at the MPA
Normal	65	3	Approximated to match measured RV stroke volume	Approximated	Reconstructed from subject MR image at end diastolic	Measured from subject MR image
PAH	44	2.93	Measured from PC-MR images	Measured from RH catheterization	Reconstructed from subject MR image at end diastolic	Measured from patient MR image

the proximal resistance, distal resistance, and compliance characteristics of the vasculature distal to that outlet.

## 2.6. Material and Windkessel model parameter calibration

Linearized stiffness ( $E$ ) and Windkessel parameters ( $R_1^i, R_2^i, C^i$ ) in each outlet  $i$  were iteratively calibrated to match the pressure-displacement relationship and pressure waveforms in both subjects (Fig. 1). These parameters were initialized using pressure, flow and geometry data. Specifically, the linearized stiffness  $E$  was estimated from a 1D elastic tube model (Matthys et al., 2007),

$$P_{sys} = P_{ED} + \frac{4}{3} \frac{\sqrt{\pi}}{A_{MPA}(t_{ED})} Eh \left( \sqrt{A_{MPA}(t_{sys})} - \sqrt{A_{MPA}(t_{ED})} \right), \quad (1)$$

where  $P_{sys}$ ,  $P_{ED}$ ,  $h$ , and  $A_{MPA}(t)$  denote, respectively, the systolic pressure, diastolic pressure, wall thickness and MPA cross sectional area at peak-systole ( $t_{sys}$ ) and ED ( $t_{ED}$ ). The Windkessel model parameters were initialized based on the following estimates of total arterial resistance  $R_T$  and compliance  $C_T$ :

$$R_T = R_1^i + R_2^i = \frac{P_{mean}}{Q_{mean}}; \quad C_T = \frac{Q_{max} - Q_{min}}{P_{sys} - P_{ED}} \Delta t. \quad (2a, b)$$

In the above equation,  $P_{mean}$ ,  $Q_{max}$ ,  $Q_{min}$ ,  $Q_{mean}$  and  $\Delta t$  denote the mean pressure, maximum, minimum, and mean volumetric flow rate, and the time interval between maximum and minimum flow in the MPA, respectively. Estimated values of  $R_T$  and  $C_T$  were then distributed to each outlet  $i$  to ensure equal flow split between the LPA and RPA using the following equations (Xiao et al., 2014):

$$R_T^{LPA} = R_T^{RPA} = \frac{P_{mean}}{\left(\frac{1}{2}\right)Q_{mean}} = 2R_T; \quad \frac{1}{R_T^i} = \left(\frac{A^i}{A_T}\right) \left(\frac{1}{2R_T}\right), \quad (3a, b)$$

$$C_T^{LPA} = C_T^{RPA} = \left(\frac{C_T}{2}\right); \quad C^i = \left(\frac{C_T}{2}\right) \cdot \left(\frac{A^i}{A_T}\right). \quad (4a, b)$$

Here,  $R_T^i, R_T^{LPA}, R_T^{RPA}, C^i, C_T^{LPA}, C_T^{RPA}, A^i$  and  $A_T$  denote, respectively, the total resistance associated with outlet  $i$ , LPA, RPA; the compliance associated with outlet  $i$ , LPA, RPA; the area of outlet  $i$ , and the total outlet area of the branches associated with either the LPA or RPA.

The total resistance at each outlet ( $R_T^i$ ) was divided into proximal and distal resistances ( $R_1^i, R_2^i$ ). The proximal resistance ( $R_1^i$ ; Eq. (5)) was assumed to match the characteristic impedance at the proximal MPA and, therefore, was prescribed with the same value at each outlet. The distal resistance ( $R_2^i$ ; Eq. (6)) was obtained by subtracting  $R_1^i$  from  $R_T^i$ , i.e.,

$$R_1^i = \frac{\rho c_{ED}}{A_{MPA}(t_{ED})}; \quad c_{ED}^2 = \frac{\left(\frac{2}{3}\right)\sqrt{\pi}Eh}{\rho\sqrt{A_{MPA}(t_{ED})}}, \quad (5a, b)$$

$$R_2^i = R_T^i - R_1^i, \quad (6)$$

where  $\rho$  and  $c_{ED}$  denote the fluid density and ED pulse wave propagation speed, respectively.

After the parameters were initialized as described above, calibration was performed iteratively in two nested loops. In the inner loop,  $R_1^i, R_2^i$  and  $C^i$  were estimated iteratively by adjusting the total resistance ( $R_T$ ) and compliance ( $C_T$ ) at the main pulmonary artery until measured values of pulse ( $\Delta P_p = P_{sys} - P_{ED}$ ) and diastolic pressures ( $P_{ED}$ ) were achieved. The iterative adjustment process was performed using the following mathematical formulation (Xiao et al., 2014).

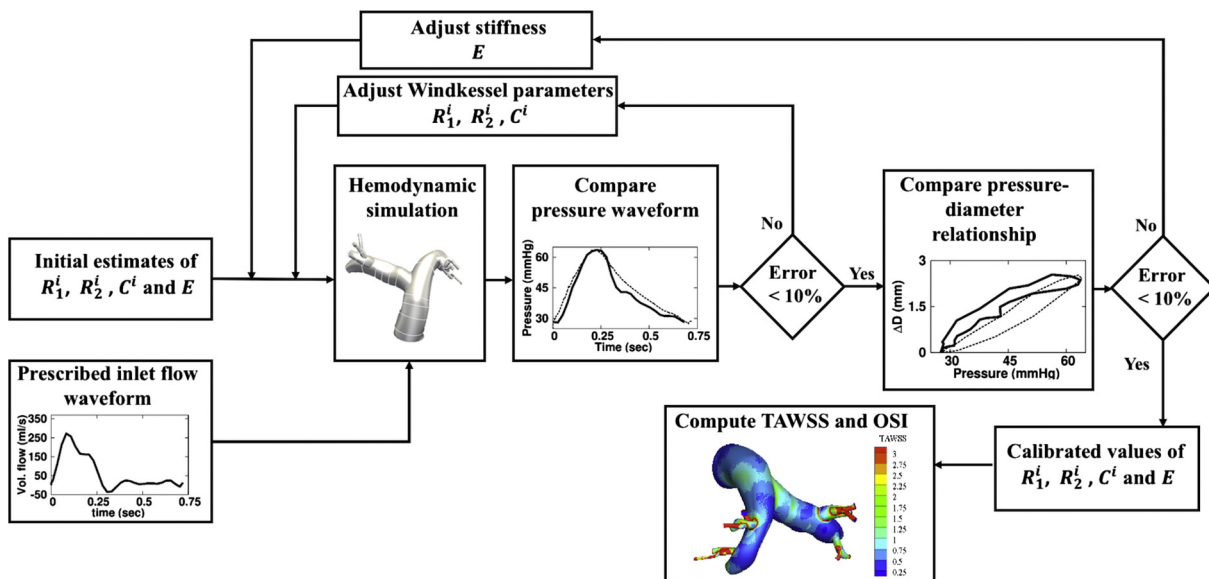


**Fig. 1.** Schematic of the model calibration process (for parameters  $R_1^i, R_2^i, C^i$  and  $E$ ) with measured pressure and diameter data.

$$R_T^{n+1} = R_T^n + \frac{\Delta P^n}{Q_{mean}} \quad \text{and} \quad C_T^{n+1} = C_T^n + \frac{Q_{max} - Q_{min}}{(P_{sys} - P_{ED})^2} \Delta t \Delta P_p^n \quad (7a, b)$$

where  $\Delta P^n$  represents the difference between measured and simulated diastolic pressure ( $P_{ED} - P_{ED}^n$ ), and  $\Delta P_p^n$  is the difference between measured and estimated pulse pressure. In the outer loop, the linearized stiffness  $E$  was calibrated to match measured pressure-displacement relationships (Fig. 1). Each loop was terminated when relative differences between the measured and simulated quantities fell below 10%. Forward simulation in each loop was performed until a truly periodic solution was attained, specifically, when the difference between the blood volume entering the domain ( $Q_i$ ) minus the summation of blood volume leaving all outlets over one cardiac cycle is less than  $10^{-3}$  ml.

### 2.7. Parametric study on the proximal and distal effect on pressure waveform

The computational framework presented here also enabled us to separate the effect of the proximal arterial stiffness, distal resistance and compliance on the pressure waveform and pulse pressure. This parametric study was performed by substituting calibrated values of linearized stiffness ( $E$ ), or distal pulmonary resistance and compliance ( $R_T, C_T$ ) of the normal model into the PAH model. Simulation was run with the switched parameters for several cardiac cycles until a periodic solution was attained as described in the previous section.

## 3. Results

### 3.1. Geometry and hemodynamics data in the pulmonary vasculature

Data revealed substantial differences in the PA geometry between the PAH patient and the normal subject (Fig. 2). Specifically, equivalent diameter at ED was larger in the PAH patient than in the normal subject: diameters in the PAH patient were 18.20%, 31.55% and 39.25% larger in the MPA, RPA and LPA, respectively. Conversely, maximum MPA diameter change (measured close to the bifurcation point) was lower in the PAH patient than that in the normal subject (2.50 vs. 4.00 mm) (Fig. 3c).

In terms of hemodynamics, measured MPA peak pressure in the PAH patient was substantially higher than typical values found in healthy subjects (62 vs. 30 mm Hg; Lankhaar et al., 2006) (Fig. 3a). Measured mean MPA volumetric flow rate in the PAH

patient was, however, lower than that measured in the normal subject (61.65 vs. 93.17 ml/s) (Fig. 3b). Slope and area enclosed in the measured pressure-displacement curve were, respectively, larger and smaller in the PAH subject (Fig. 3c).

### 3.2. Calibrated model parameters

Because we did not see significant differences in the results between using a blunt and a parabolic velocity profile, all subsequent results reported here are based on the blunt velocity profile. Calibrated values of linearized stiffness  $E$  were 2.0 and 0.50 MPa (Fig. 4) in the PAH and normal models, respectively. Calibrated total distal flow resistance  $R_T$  was 11.3 mmHg\*min/l in the PAH model and 2.6 mmHg\*min/l in the normal model, whereas calibrated total distal compliance  $C_T$  was 0.3 ml/mmHg in the PAH model and 2.9 ml/mmHg in the normal model (Fig. 4). Using the calibrated parameter values, the maximum differences between measurements and model predictions in time-averaged pressure, peak pressure and peak diameter were within 4.12%, 6.80% and 4.70% for both subjects.

Time-averaged wall shear stress (TAWSS) and oscillatory shear index (OSI) were computed. Larger TAWSS and smaller OSI were observed at the MPA when compared to the smaller branches (Fig. 5a) in both models. Circumferential averaged TAWSS was lower in the PAH model at all locations along the 3 main branches of the PA (i.e., MPA, RPA and LPA). On the other hand, OSI was higher along all the branches in the PAH model (Fig. 5b). Averaged over the entire PA geometry, TAWSS and OSI in the PAH model were found, respectively, to be 1.4 and 0.18 Pa. In the normal model, TAWSS and OSI were found to be 4.2 and 0.08 Pa, respectively (Fig. 5c).

### 3.3. Model prediction of PA wall mechanical behavior

Radial displacement of the PA wall was substantially lower in the PAH model (Fig. 6a and b). Quantified as changes in equivalent diameter along the vessel (Fig. 2), the largest displacement was located at the MPA in the normal model and decreased slightly along the LPA and RPA. Conversely, radial displacement was uniform but substantially smaller in the PAH model from the mid-section of the MPA to that in the LPA and RPA. Average displacement of the entire PA in the PAH model (1.69 mm) was about 36% smaller than in the normal model (2.63 mm).

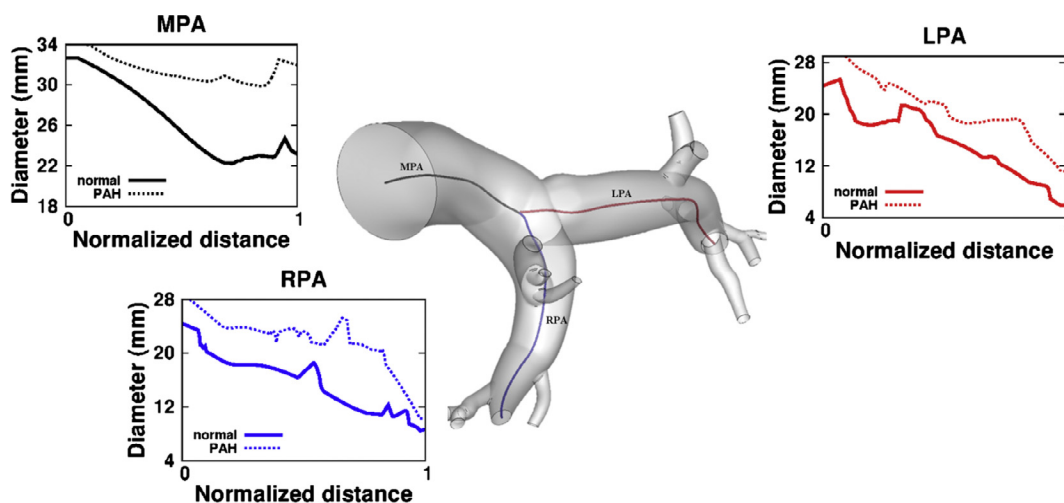


Fig. 2. Profile of the diameter measured along the centerline of the pulmonary arteries at ED in the PAH patient and normal subject.

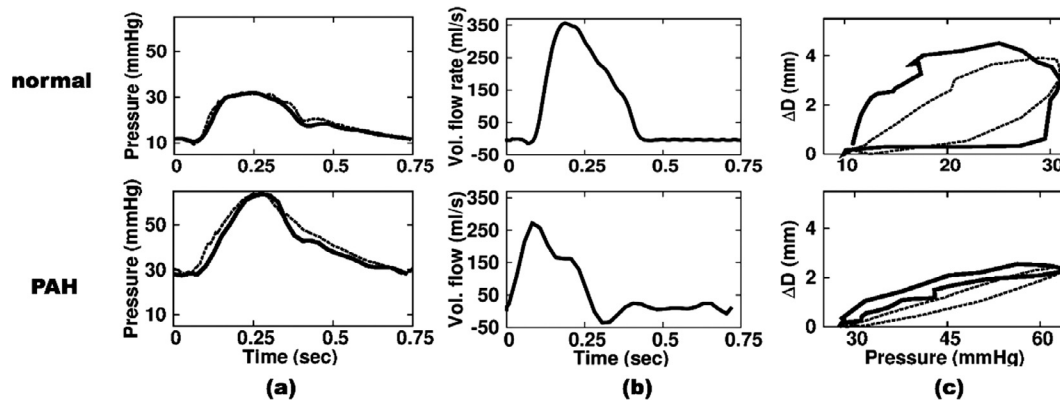


Fig. 3. Measurements (solid lines) and model predictions (dotted lines) of: (a) pressure, (b) volumetric flow rate, and (c) pressure-displacement curves for the normal subject (top) and PAH patient (bottom).

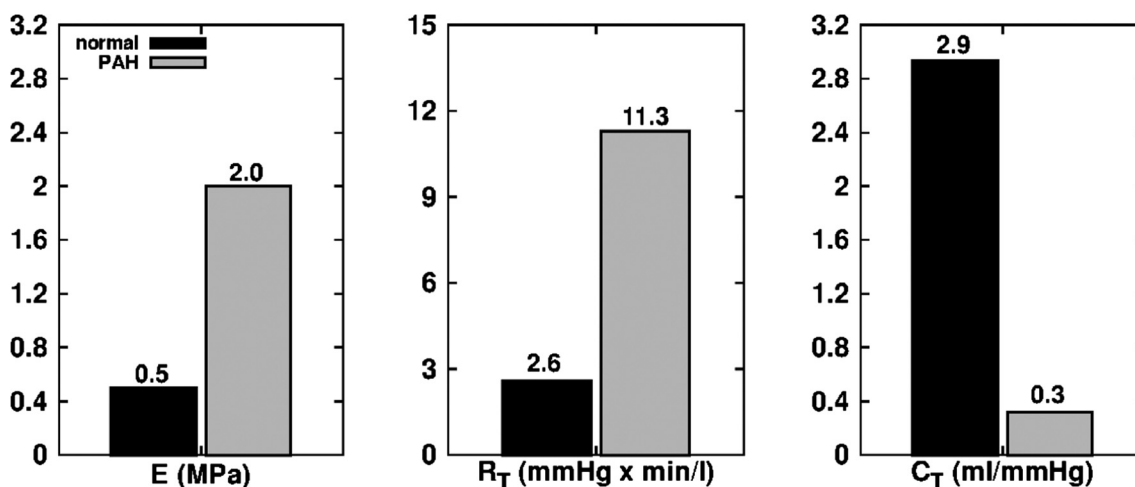


Fig. 4. Comparison of calibrated values of the proximal linearized stiffness  $E$ , total distal resistance  $R_T$  and compliance  $C_T$  between normal and PAH subject.

Relative area change (RAC), a metric shown to be strongly correlated with mortality in PAH (Gan et al., 2007), was also computed along the main, left and right pulmonary artery (Fig. 6c). This metric is defined as the maximum area change divided by the area at end systolic ( $A_{\max \text{ disp}} - A_{\text{ED}}/A_{\text{ED}}$ ). Our results showed lower RAC in the PAH model ( $\sim 0.14$ ) when compared to the normal model ( $\sim 0.31$ ) along all three branches (MPA, LPA and RPA).

Fig. 7 shows the differences in pulse wave propagation along the MPA and its branches between the normal and the PAH subject. The pressure waveforms revealed a noticeable phase lag between different locations in the MPA, RPA and LPA of the normal model. This phase lag was entirely absent in the PAH model. This disparity is associated with a much higher pulse wave velocity estimated in the PAH model (5.6 m/s) than the normal model (2.7 m/s) because of the higher tissue stiffness and thickness in the former.

#### 3.4. Effects of proximal and distal parameters on the pressure waveform

Pulse pressure is a hemodynamic metric that has been shown to be strongly correlated with arterial remodeling (Coogan et al., 2013; Eberth et al., 2009), and its ratio with stroke volume has been shown to be a strong independent predictor of mortality in idiopathic PAH patients (Mahapatra et al., 2006). The effect of substituting calibrated parameter values associated with the proximal

( $E$ ) and distal pulmonary vasculature ( $R_T$ ,  $C_T$ ) found in the normal model into the PAH model (Fig. 8) was investigated using this metric. Substituting the linearized stiffness with the values found in the normal model led to a decrease in 52.49% in the pulse pressure. Similarly, substituting calibrated values of the total distal resistance  $R_T$  and compliance  $C_T$  values found in the normal model into the PAH model led to a larger decrease of 60.94% compared to the measured pulse pressure.

#### 4. Discussion

We have developed patient-specific computational models of hemodynamics in the pulmonary vasculature using measurements acquired from a PAH patient and a normal subject. These models included the fluid-structure interactions between blood flow and arterial wall, therefore overcoming a key limitation of previous computational models of PAH (Kheifets et al., 2015, 2013; Su et al., 2013). We investigated both hemodynamics and mechanical behavior of the large pulmonary arteries. We have calibrated the PAH model against *in vivo* patient-specific measurements of blood flow, pressure and vessel wall deformation. For the normal model, calibration was performed using flow and pressure measurements from health subjects in a previous study together with patient-specific measurements of vessel wall deformation. The model parameters consist of the linearized stiffness  $E$  of the large vessels,

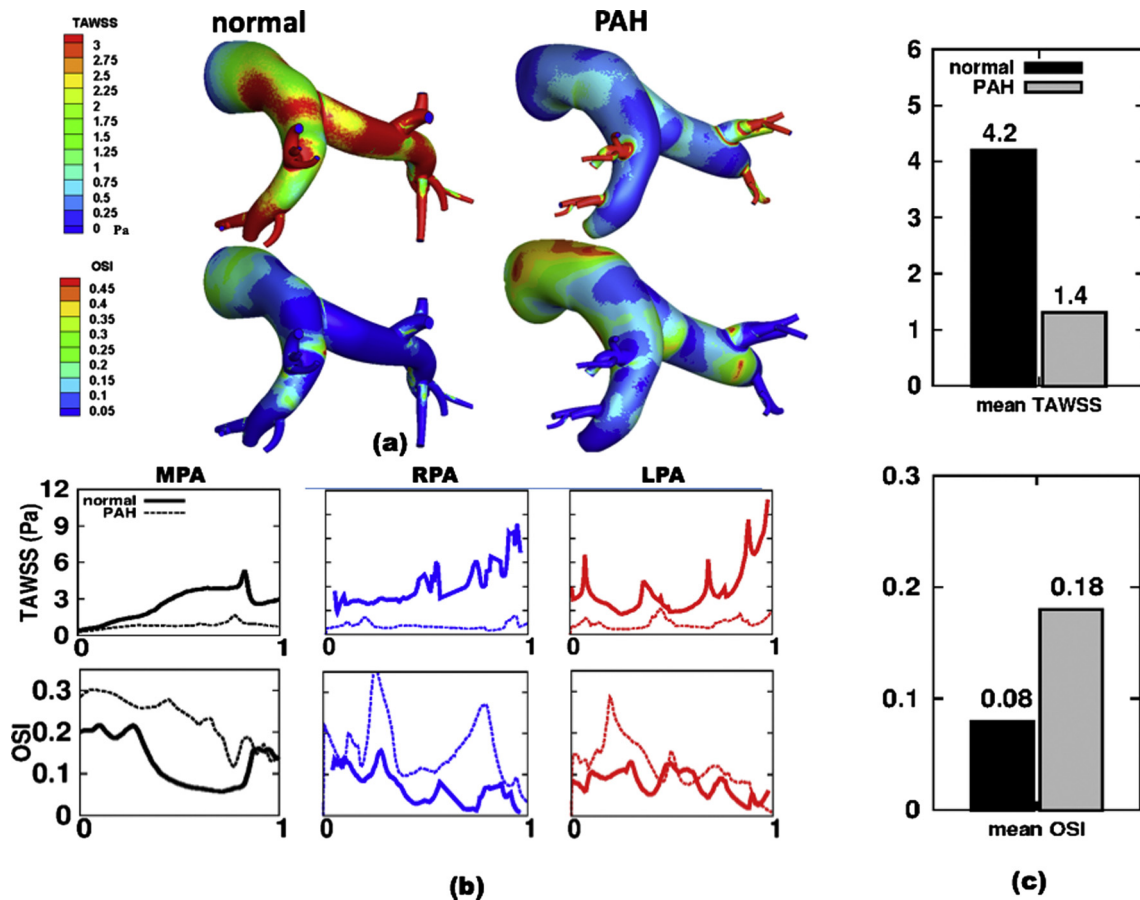


**Fig. 5.** Comparison of (a) spatial distribution (b) circumferentially average of TAWSS and OSI plotted with the normalized distance in MPA, RPA and LPA; and (c) mean values of TAWSS and OSI between the normal and PAH subject.

and the Windkessel parameters reflecting compliance and flow resistance of the distal vessels.

Calibrated linearized stiffness in the large vessels (MPA, LPA and RPA) were found to be 2.0 and 0.5 MPa in the PAH and normal models, respectively. The large stiffness found in the PAH model was also reflected by the low RAC value, a parameter strongly correlated with mortality (Gan et al., 2007). These results are in agreement with previous human studies (Lau et al., 2012; Sanz et al., 2009), which also found that the PA is substantially stiffer in PAH patients (Lau et al., 2012; Stevens et al., 2012). Lau et al. (2012) found that the linearized stiffness of the proximal PA (based on a different definition) is on average 3.6 times higher in PAH patients than in healthy subjects. We note that while the model predicted an increase in stiffness in the PAH patient, it cannot differentiate whether its increase is caused by arterial remodeling (e.g., fibrosis) or simply, by the nonlinearity mechanical behavior of the artery. The study by Tian et al. (2014) clearly shows that the increase in stiffness found in acute PAH is associated with the latter mechanism. With remodeling (most probably in the case of PAH patient), however, the dominant mechanism becomes less clear. For example, a study using chronic monocrotaline-induced PAH rat model have found that the collagen content increases, the collagen fiber becomes less wavy, and the PA Young's modulus correspondingly increases at 4 weeks (Pursell et al., 2016).

Distal vasculature in the PAH model was found to possess a total compliance  $C_T$  of 0.32 ml/mmHg and resistance  $R_T$  of 11.3 mmHg\*min/l. These parameters are statistically associated with

higher mortality in PAH patients (Gan et al., 2007; Mahapatra et al., 2006). The larger value of total resistance  $R_T$  found in the PAH model suggests that the distal pulmonary vessels are more constricted. These results are consistent with histologic studies (Barberà et al., 1994; Santos et al., 2002; Shimoda and Laurie, 2013) on samples acquired from PAH patients that revealed a decrease in distal lumen size and intimal thickening, both indicative of stiffer vessels.

Time-averaged wall shear stress and OSI were, respectively, lower and higher along the MPA and RPA in the PAH model. Our results are comparable to the range of values found in previous computational studies using PAH subjects data (Kheyfets et al., 2015; Tang et al., 2012) (mean TAWSS: 1.4 Pa) and healthy subjects data (Tang et al., 2012) (mean TAWSS: 4.2 Pa). Our results revealed a noticeable phase shift in pressure waveforms at different locations of the MPA in the normal subject. This shift was absent in the PAH subject. Pressure-displacement relationship was also different between the PAH and the normal model with the latter having a larger area inside the curve. These features, which can be largely attributed to the smaller compliance found in the PAH model, has also been observed in a previous animal study (Wang et al., 2013).

Substituting the parameter values of  $E$  and  $(C_T, R_T)$  in the PAH model with those found in the normal model allowed us to quantify the effects on pulse pressure resulting from alterations in the proximal or distal vasculature. A decrease in the pulse pressure was found when values of  $(C_T, R_T)$  from the normal model were

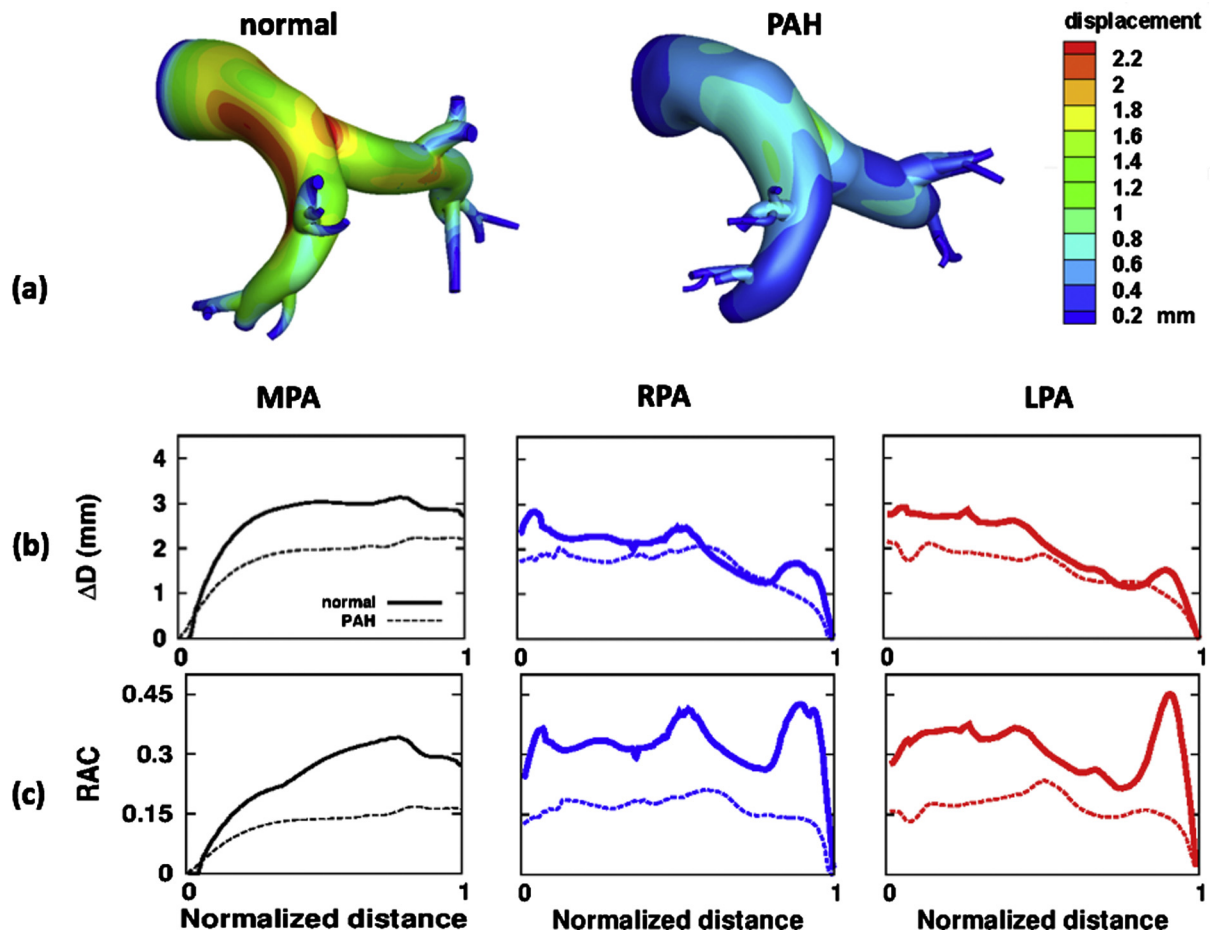


**Fig. 6.** Comparison of (a): spatial distribution of the maximum radial displacement and (b) maximum diameter change and (c) RAC along the MPA, RPA and LPA in the normal and PAH model.

used in the PAH model. This decrease is larger than when the value of  $E$  in the normal model was used. This result suggests that remodeling in the distal vasculature accounts for a larger portion of the increase in RV workload found in PAH patients (Chemla et al., 2013).

#### 4.1. Limitations

The computational framework presented here overcomes some drawbacks of previous modeling efforts to analyze PAH. Nevertheless, there are still some limitations. First, the coupled momentum formulation assumes that the vessel wall behaves in a linear elastic manner and undergoes small deformations. Therefore, the description of vessel wall mechanics in the model is essentially a first-order approximation. Second, we have assumed homogenous values of linearized stiffness for the entire pulmonary vasculature. Regional data on localized stiffness could be used to circumvent this limitation. Third, the segmented geometry, particularly at the smaller branches and bifurcations, may not be accurate because of the resolution of clinical MR images is limited. This error may affect the estimation of hemodynamic quantities and the model parameters. Fourth, flow and pressure data were not acquired in the pulmonary artery of the normal subject, as the latter requires invasive RHC. To circumvent this issue, we have used pressure and flow waveforms acquired in previous studies of normal humans as surrogate data in our study. We have also scaled

the flow waveform so that total outflow in the MPA is the same as the RV stroke volume measured in the normal subject. Fifth, we have fixed the inlet and outlet boundaries in our models as in previous studies (Figueroa et al., 2006). Axial motion, however, may occur in the pulmonary arteries even though distensibility in the axial direction has been found to be lower compared to the radial direction (Bellofiore et al., 2015). Correspondingly, this assumption may lead to some error. Finally, the proposed computational hemodynamic framework was applied only to data acquired from a normal subject and a PAH patient. Moreover, the parametric study to assess the impact of model parameters on pressure waveform was performed only on 3 parameters ( $E, R_T, C_T$ ) with no intermediate values. Conclusions drawn from this study will be strengthened by applying the framework to a larger patient dataset and including more parameters. Nevertheless, results obtained using the proposed computational model are in agreement with previous findings

#### 4.2. Conclusion

The modeling framework described here represents an advancement in computational analysis of PAH hemodynamics, particularly, in the simultaneous quantification of changes in hemodynamics and vessel wall mechanics associated with this disease. This framework will be applied in future studies to quantify the mechanical impact of PAH on the pulmonary vasculature.

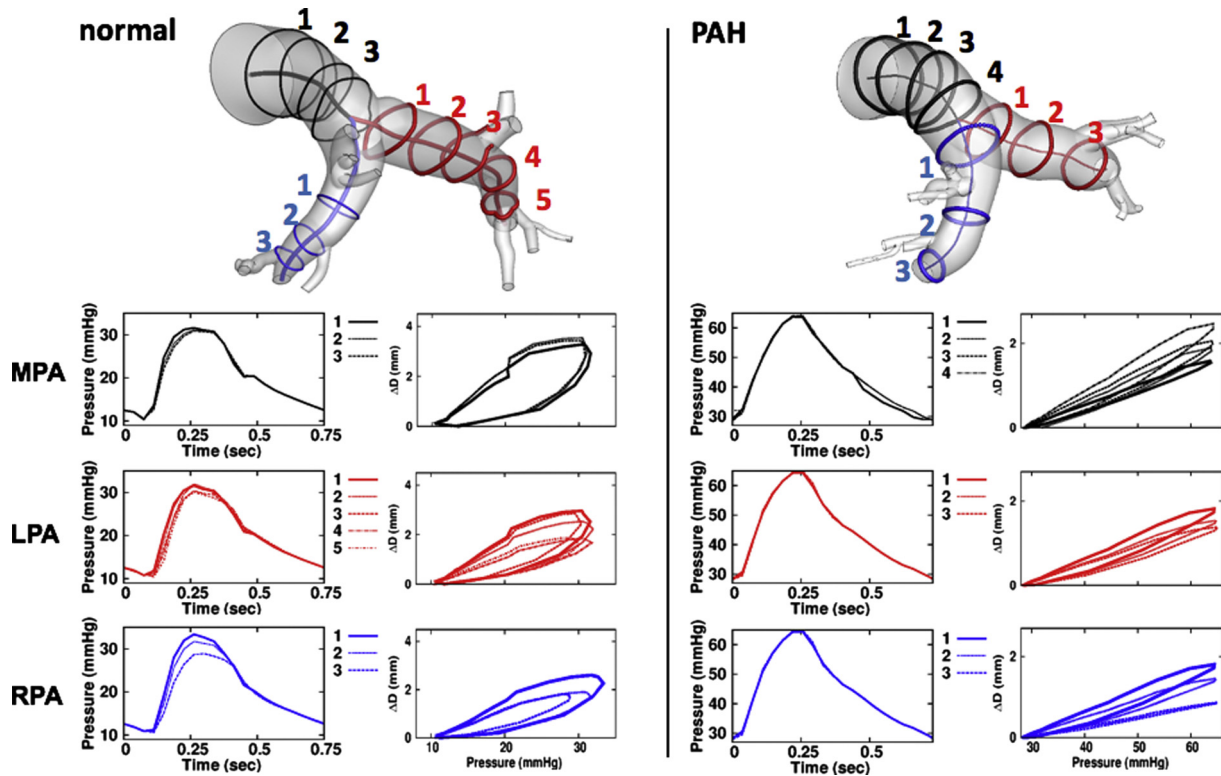


Fig. 7. Comparison of the variation of pressure waveform and changes in pressure-displacement relationship at different cross sections along the MPA (black), LPA (red) and RPA (blues) between the PAH patient and normal subject. (For interpretation of the references to colour in this figure legend, the reader is referred to the web version of this article.)

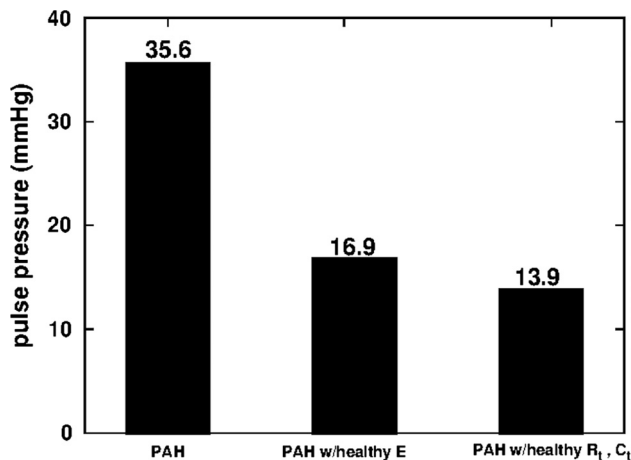


Fig. 8. Effects on the pulse pressure in the PAH model when values of linearized stiffness  $E$  and the Windkessel parameters ( $C_T, R_T$ ) were replaced by those found in the normal model.

**Acknowledgement**

This study was supported by NSF CAREER (CMMI-1150376, Baek), Singapore Ministry of Health’s National Medical Research Council (NMRC/OFIRG/0018/2016, Zhong), Goh Cardiovascular Research Award (Duke-NUS-GCR/2013/0009, Zhong), AHA SDG (17SDG33370110, Lee), the European Research Council under the European Union’s Seventh Framework Programme (FP/2007-2013)/ERC Grant Agreement no. 307532 and NIH (U01 1HL135842, Figueroa, Baek and Lee).

**Conflict of interest**

No conflicts of interest, financial or otherwise, are declared by the authors.

**Appendix A. Supplementary data**

Supplementary data associated with this article can be found, in the online version, at <https://doi.org/10.1016/j.jbiomech.2017.12.022>.

**References**

Barberà, J.A., Riverola, A., Roca, J., Ramirez, J., Wagner, P.D., Ros, D., Wiggs, B.R., Rodriguez-Roisin, R., 1994. Pulmonary vascular abnormalities and ventilation-perfusion relationships in mild chronic obstructive pulmonary disease. *Am. J. Respir. Crit. Care Med.* 149, 423–429. <https://doi.org/10.1164/ajrccm.149.2.8306040>.

Bellinazzi, V.R., Cipolli, J.A., Pimenta, M.V., Guimarães, P.V., Pio-Magalhães, J.A., Coelho-Filho, O.R., Biering-Sørensen, T., Matos-Souza, J.R., Sposito, A.C., Nadruz, W., 2015. Carotid flow velocity/diameter ratio is a predictor of cardiovascular events in hypertensive patients. *J. Hypertens.* 33, 2054–2060. <https://doi.org/10.1097/HJH.0000000000000688>.

Bellofiore, A., Henningsen, J., Lepak, C.G., Tian, L., Roldan-Alzate, A., Kelliham, H.B., Consigny, D.W., Francois, C.J., Chesler, N.C., 2015. A novel in vivo approach to assess radial and axial distensibility of large and intermediate pulmonary artery branches. *J. Biomech. Eng.* 137–141, 44501. <https://doi.org/10.1115/1.4029578>.

Chemla, D., Castelain, V., Zhu, K., Papelier, Y., Creuzé, N., Hoette, S., Parent, F., Simonneau, G., Humbert, M., Herve, P., 2013. Estimating right ventricular stroke work and the pulsatile work fraction in pulmonary hypertension. *Chest* 143, 1343–1350. <https://doi.org/10.1378/chest.12-1880>.

Coogan, J.S., Humphrey, J.D., Figueroa, C.A., 2013. Computational simulations of hemodynamic changes within thoracic, coronary, and cerebral arteries following early wall remodeling in response to distal aortic coarctation. *Biomech. Model. Mechanobiol.* 12, 79–93. <https://doi.org/10.1007/s10237-012-0383-x>.

- Cuomo, F., Ferruzzi, J., Humphrey, J.D., Figueroa, C.A., 2015. An experimental-computational study of catheter induced alterations in pulse wave velocity in anesthetized mice. *Ann. Biomed. Eng.* 43, 1555–1570. <https://doi.org/10.1007/s10439-015-1272-0>.
- Cuomo, F., Roccabianca, S., Dillon-Murphy, D., Xiao, N., Humphrey, J.D., Figueroa, C.A., 2017. Effects of age-associated regional changes in aortic stiffness on human hemodynamics revealed by computational modeling. *PLoS ONE* 12. <https://doi.org/10.1371/journal.pone.0173177>.
- Eberth, J.F., Gresham, V.C., Reddy, A.K., Popovic, N., Wilson, E., Humphrey, J.D., 2009. Importance of pulsatility in hypertensive carotid artery growth and remodeling. *J. Hypertens.* 27, 2010–2021. <https://doi.org/10.1097/HJH.0b013e32832e8dc8>.
- Figueroa, C.A., Vignon-Clementel, I.E., Jansen, K.E., Hughes, T.J.R., Taylor, C.A., 2006. A coupled momentum method for modeling blood flow in three-dimensional deformable arteries. *Comput. Meth. Appl. Mech. Eng.* 195, 5685–5706. <https://doi.org/10.1016/j.cma.2005.11.011>.
- Gan, C.T.-J., Lankhaar, J.-W., Westerhof, N., Marcus, J.T., Becker, A., Twisk, J.W.R., Boonstra, A., Postmus, P.E., Vonk-Noordegraaf, A., 2007. Noninvasively assessed pulmonary artery stiffness predicts mortality in pulmonary arterial hypertension. *Chest* 132, 1906–1912. <https://doi.org/10.1378/chest.07-1246>.
- Gharahi, H., Zambrano, B.A., Lim, C., Choi, J., Lee, W., Baek, S., 2015. On growth measurements of abdominal aortic aneurysms using maximally inscribed spheres. *Med. Eng. Phys.* 37, 683–691. <https://doi.org/10.1016/j.medengphy.2015.04.011>.
- Hislop, A., Reid, L., 1978. Normal structure and dimensions of the pulmonary arteries in the rat. *J. Anat.* 125, 71–83.
- Hunter, K.S., Lanning, C.J., Chen, S.-Y.J., Zhang, Y., Garg, R., Ivy, D.D., Shandas, R., 2006. Simulations of congenital septal defect closure and reactivity testing in patient-specific models of the pediatric pulmonary vasculature: a 3D numerical study with fluid-structure interaction. *J. Biomech. Eng.* 128, 564–572. <https://doi.org/10.1115/1.2206202>.
- Jakrapanichakul, D., Chirakarnjanakorn, S., 2011. Comparison of aortic diameter in normal subjects and patients with systemic hypertension. *J. Med. Assoc. Thai. Chotmaihet Thangphaet* 94 (Suppl 1), S51–S56.
- Keyfets, V.O., O'Dell, W., Smith, T., Reilly, J.J., Finol, E.A., 2013. Considerations for numerical modeling of the pulmonary circulation—a review with a focus on pulmonary hypertension. *J. Biomech. Eng.* 135, 61011–61015. <https://doi.org/10.1115/1.4024141>.
- Keyfets, V.O., Rios, L., Smith, T., Schroeder, T., Mueller, J., Murali, S., Lasorda, D., Zikos, A., Spotti, J., Reilly, J.J., Finol, E.A., 2015. Patient-specific computational modeling of blood flow in the pulmonary arterial circulation. *Comput. Meth. Prog. Biomed.* 120, 88–101. <https://doi.org/10.1016/j.cmpb.2015.04.005>.
- Khlebnikov, R., Figueroa, C.A., 2015. CRIMSON: towards a software environment for patient-specific blood flow simulation for diagnosis and treatment. In: *Clinical Image-Based Procedures. Translational Research in Medical Imaging*. Presented at the Workshop on Clinical Image-Based Procedures, Springer, Cham, pp. 10–18, doi:10.1007/978-3-319-31808-0\_2.
- Kung, E.O., Les, A.S., Figueroa, C.A., Medina, F., Arcaute, K., Wicker, R.B., McConnell, M.V., Taylor, C.A., 2011. In vitro validation of finite element analysis of blood flow in deformable models. *Ann. Biomed. Eng.* 39, 1947–1960. <https://doi.org/10.1007/s10439-011-0284-7>.
- Lankhaar, J.-W., Westerhof, N., Faes, T.J.C., Marques, K.M.J., Marcus, J.T., Postmus, P.E., Vonk-Noordegraaf, A., 2006. Quantification of right ventricular afterload in patients with and without pulmonary hypertension. *Am. J. Physiol. Heart Circ. Physiol.* 291, H1731–H1737. <https://doi.org/10.1152/ajpheart.00336.2006>.
- Lau, E.M.T., Iyer, N., Ihsar, R., Bailey, B.P., Adams, M.R., Celermaier, D.S., 2012. Abnormal pulmonary artery stiffness in pulmonary arterial hypertension: In vivo study with intravascular ultrasound. *PLoS ONE* 7. <https://doi.org/10.1371/journal.pone.0033331>.
- Mahapatra, S., Nishimura, R.A., Sorajja, P., Cha, S., McGoan, M.D., 2006. Relationship of pulmonary arterial capacitance and mortality in idiopathic pulmonary arterial hypertension. *J. Am. Coll. Cardiol.* 47, 799–803. <https://doi.org/10.1016/j.jacc.2005.09.054>.
- Matthys, K.S., Alastruey, J., Peiró, J., Khir, A.W., Segers, P., Verdonck, P.R., Parker, K.H., Sherwin, S.J., 2007. Pulse wave propagation in a model human arterial network: assessment of 1-D numerical simulations against in vitro measurements. *J. Biomech.* 40–46, 3476–3486. <https://doi.org/10.1016/j.jbiomech.2007.05.027>.
- McLaughlin, V.V., Archer, S.L., Badesch, D.B., Barst, R.J., Farber, H.W., Lindner, J.R., Mathier, M.A., McGoan, M.D., Park, M.H., Rosenson, R.S., Rubin, L.J., Tapson, V.F., Varga, J., 2009. ACCF/AHA 2009 expert consensus document on pulmonary hypertension: a report of the American college of cardiology foundation task force on expert consensus documents and the American heart association: developed in collaboration with the American College. *Circulation* 119, 2250–2294. <https://doi.org/10.1161/CIRCULATIONAHA.109.192230>.
- Pursell, E.R., Vélez-Rendón, D., Valdez-Jasso, D., 2016. Biaxial properties of the left and right pulmonary arteries in a monocrotaline rat animal model of pulmonary arterial hypertension. *J. Biomech. Eng.* 138–149. <https://doi.org/10.1115/1.4034826>.
- Santos, S., Peinado, V.I., Ramírez, J., Melgosa, T., Roca, J., Rodríguez-Roisin, R., Barberà, J.A., 2002. Characterization of pulmonary vascular remodelling in smokers and patients with mild COPD. *Eur. Respir. J.* 19, 632–638. <https://doi.org/10.1183/09031936.02.00245902>.
- Sanz, J., Kariisa, M., Dellegrattaglia, S., Prat-González, S., Garcia, M.J., Fuster, V., Rajagopalan, S., 2009. Evaluation of pulmonary artery stiffness in pulmonary hypertension with cardiac magnetic resonance. *JACC Cardiovasc. Imaging* 2, 286–295. <https://doi.org/10.1016/j.jcmg.2008.08.007>.
- Shimoda, L.A., Laurie, S.S., 2013. Vascular remodeling in pulmonary hypertension. *J. Mol. Med. Berl. Ger.* 91, 297–309. <https://doi.org/10.1007/s00109-013-0998-0>.
- Stenmark, K.R., Meyrick, B., Galie, N., Mooi, W.J., McMurtry, I.F., 2009. Animal models of pulmonary arterial hypertension: the hope for etiological discovery and pharmacological cure. *Am. J. Physiol. Lung Cell. Mol. Physiol.* 297, L1013–L1032. <https://doi.org/10.1152/ajplung.00217.2009>.
- Stevens, G.R., Garcia-Alvarez, A., Sahni, S., Garcia, M.J., Fuster, V., Sanz, J., 2012. RV dysfunction in pulmonary hypertension is independently related to pulmonary artery stiffness. *JACC Cardiovasc. Imag.* 5, 378–387. <https://doi.org/10.1016/j.jcmg.2011.11.020>.
- Su, Z., Hunter, K.S., Shandas, R., 2012. Impact of pulmonary vascular stiffness and vasodilator treatment in pediatric pulmonary hypertension: 21 patient-specific fluid-structure interaction studies. *Comput. Meth. Programs Biomed.* 108, 617–628. <https://doi.org/10.1016/j.cmpb.2011.09.002>.
- Su, Z., Tan, W., Shandas, R., Hunter, K.S., 2013. Influence of distal resistance and proximal stiffness on hemodynamics and RV afterload in progression and treatments of pulmonary hypertension: a computational study with validation using animal models. *Comput. Math. Meth. Med.* 2013, 618326. <https://doi.org/10.1155/2013/618326>.
- Sutendra, G., Michelakis, E.D., 2013. Pulmonary arterial hypertension: challenges in translational research and a vision for change. *Sci. Transl. Med.* 5, 208sr5. <https://doi.org/10.1126/scitranslmed.3005428>.
- Tang, B.T., Pickard, S.S., Chan, F.P., Tsao, P.S., Taylor, C.A., Feinstein, J.A., 2012. Wall shear stress is decreased in the pulmonary arteries of patients with pulmonary arterial hypertension: an image-based, computational fluid dynamics study. *Pulm. Circ.* 2, 470–476. <https://doi.org/10.4103/2045-8932.105035>.
- Tian, L., Kelliham, H.B., Henningsen, J., Bellofiore, A., Forouzan, O., Roldán-Alzate, A., Consigny, D.W., Gunderson, M., Dailey, S.H., Francois, C.J., Chesler, N.C., 2014. Pulmonary artery relative area change is inversely related to ex vivo measured arterial elastic modulus in the canine model of acute pulmonary embolization. *J. Biomech.* 47, 2904–2910. <https://doi.org/10.1016/j.jbiomech.2014.07.013>.
- Trip, P., Rain, S., Handoko, M.L., van der Bruggen, C., Bogaard, H.J., Marcus, J.T., Boonstra, A., Westerhof, N., Vonk-Noordegraaf, A., de Man, F.S., 2015. Clinical relevance of right ventricular diastolic stiffness in pulmonary hypertension. *Eur. Respir. J.* 45, 1603–1612. <https://doi.org/10.1183/09031936.00156714>.
- Tuder, R., Marecki, J., Richter, A., Fijalkowska, I., Flores, S., 2007. Pathology of pulmonary hypertension rubin. *Clin. Chest Med.* 28, 1–30. <https://doi.org/10.1016/j.ccm.2006.11.010>.
- Wang, Z., Lakes, R.S., Golob, M., Eickhoff, J.C., Chesler, N.C., 2013. Changes in large pulmonary arterial viscoelasticity in chronic pulmonary hypertension. *PLOS ONE* 8. <https://doi.org/10.1371/journal.pone.0078569>.
- Xiao, N., Alastruey, J., Alberto Figueroa, C., 2014. A systematic comparison between 1-D and 3-D hemodynamics in compliant arterial models. *Int. J. Numer. Meth. Biomed. Eng.* 30, 204–231. <https://doi.org/10.1002/cnm.2598>.
- Xiao, N., Humphrey, J.D., Figueroa, C.A., 2013. Multi-scale computational model of three-dimensional hemodynamics within a deformable full-body arterial network. *J. Comput. Phys. Multi-scale Model. Simul. Biol. Syst.* 244, 22–40. <https://doi.org/10.1016/j.jcp.2012.09.016>.